ARTICLE

Received 00th January 20xx,
Accepted 00th January 20xx

DOI: 10.1039/x0xx00000x

SUPPLEMENTARY INFORMATION: Diffusion kinetics of volatile organic compounds monitored by nanohole surface plasmonics

Swapnil Daxini,[a] Chris Prüfert,[b] Paul Reid,[a] Pedro Barros,[c] Juan M. Gomez-Cruz,[d] Carlos Escobedo,[e] Jack A. Barnes,[f] and Hans-Peter Loock*[g]

This document expands on the experimental details of the nebulizer design, the properties of the gold-film nanohole array (obtained by scanning electron microscopy), and the PDMS film thickness and its swelling upon o-xylene uptake. We also derive two models for the uptake and desorption of analytes into a supported film and free-standing film, respectively. Finally, we provide a FDTD calculation determining the fraction of the surface plasmon polaritons that interact with the PDMS near the holes and near the substrate, respectively.

1. Design and modelling of the nebulizer

The performance of the nebulizer is dependent on several design parameters that govern the atomization process due the presence of the shear forces at the tip of the capillary. The gas flow rate and pressure govern the velocity and shear forces where the gas interacts with the liquid stream as it exits the inner capillary. Higher gas velocities enhance droplet breakup through increased shear, resulting in finer aerosol generation, but may also lead to excessive dispersion or undesired turbulence. To investigate the performance of the nebulizer, a Computational Fluid Dynamics simulation (Autodesk CFD, USA) was performed and coupled to a finite element analysis (Fusion360) using the experimental dimensions. The results are shown in **Figure S1**.

We observe a strong velocity gradient at the tip of the inner capillary which shows the strong shear forces used to evaporate the liquid. The backing pressure was simulated as 15 bar which yields a narrow and symmetric gas flow, indicative of uniform atomization.

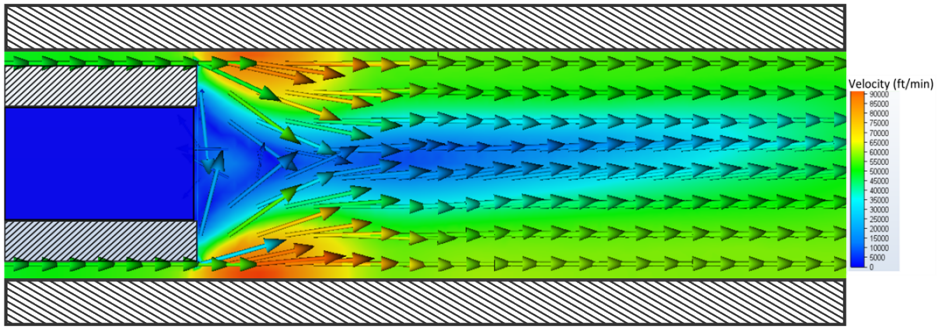

Figure S1 Computational Fluid Dynamics simulation of the coaxial nebulizer. The N_2 backing pressure is set to 15 bar which produces a N_2 gas velocity of 50,000 ft/min (or 250 m/s). The outer capillary has an inner diameter of 0.8 mm, while the inner capillary has an inner and outer diameter of 0.4 mm and 0.7 mm respectively.

[a] *Dept. of Physics, University of Victoria, Victoria, B.C., Canada V8N 5C2*
[b] *Inst. of Chemistry, Physical Chemistry, University of Potsdam, 14469 Potsdam, Germany*
[c] *Dept. of Biochemistry, University of Victoria, Victoria, B.C., Canada V8N 5C2*
[d] *Spectra Plasmonics, Kingston, ON, Canada K7L 0E9*
[e] *Dept. of Chemical Engineering, Queen's University, Kingston, ON, Canada K7L 3N6*
[f] *Dept. of Chemistry, Queen's University, Kingston, ON, Canada K7L 3N6*
[g] *Dept. of Chemistry, University of Victoria, Victoria, B.C., Canada V8N 5C2*
* hploock@uvic.ca

The outer capillary through which the N_2 gas was injected was heated to 50 °C to counteract the cooling due to evaporation and rapid expansion of the analyte. This increased the temperature of the gas at the nozzle and in the tubing downstream from -15°C to room temperature and prevented condensation of the analyte.

The range of operation of the nebulizer was determined as 10 ppm to 4000 ppm of o-xylene in N_2 by varying the flow rate and observing the onset of the formation of droplets at the output. The nebulizer was tested at different pump flow rates to determine the limit at which we do not observe complete nebulization of the solvent – apparent by the formation of droplets. Similarly, we varied the temperature of the nitrogen carrier gas to observe the onset of condensation by observing the formation of droplets at the exit of the nebulizer.

Modelling of the gas flow was used to determine the effectiveness of the nebulizer performance within that operating range.

2. Scanning electron micrograph

Figure S2 shows the scanning electron micrograph image of the nanohole array with two different magnifications (Hitachi S-4800 FESEM). The measured radius and pitch values were 100 nm and 400 nm, respectively, and are consistent with the values provided

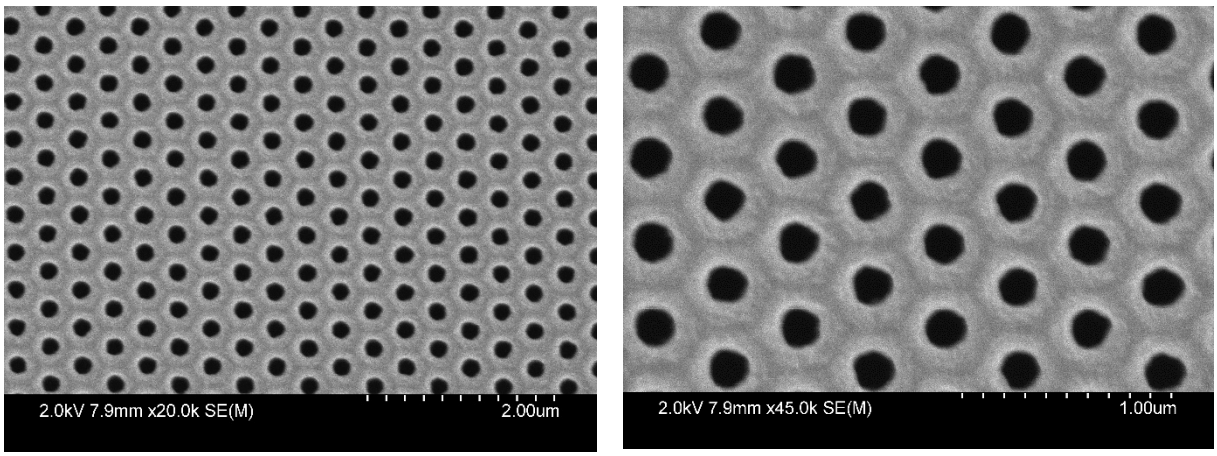

Figure S2 Scanning electron micrograph of nanohole array with x20k (left) and x45k (right) magnification. The average radius and pitch of the array was measured to be (99 ± 3) nm and (407 ± 6) nm respectively. The average pitch was measured through image analysis of the x20k magnification image to determine the spacing between the holes, while the average radius was measured from the area of the holes in the x45k magnification image to account for shape irregularities.

by the manufacturer.

3. NHA chamber

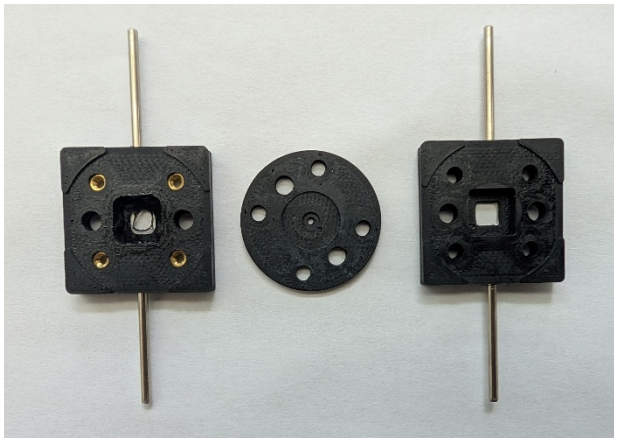

Figure S3 3D printed NHA chamber parts

The PDMS-NHA structure was enclosed in a 3D printed in-house built chamber that allows the transmission of light through the center of the chamber and allows for the gases to flow on the top and bottom of the PDMS-NHA structure. It consists of three main parts, i.e. two outer plates and one central disc that holds the NHA **Figure S3**.

The plates have a 5 mm x 5 mm square open hole that is turned into an optical window using cover glass squares (Fisher Scientific, USA) that are attached and sealed using epoxy resin. Facing inside, each plate has a square center recess that forms the sensor chamber. The sensor chamber accepts sample gas through a bore connected with 22 needle gauge tubing to the gas flow system, while the second bore directs the sample gas to waste after it has flown across the PDMS film which faces the white light source. The right part of the chamber has a similar design and would permit gas flow across the silicon nitride grid that forms the support for the NHA assembly.

4. PDMS thickness calibration

The spin-coater was calibrated to produce reproducible PDMS film thickness. The film thickness was determined for different spin

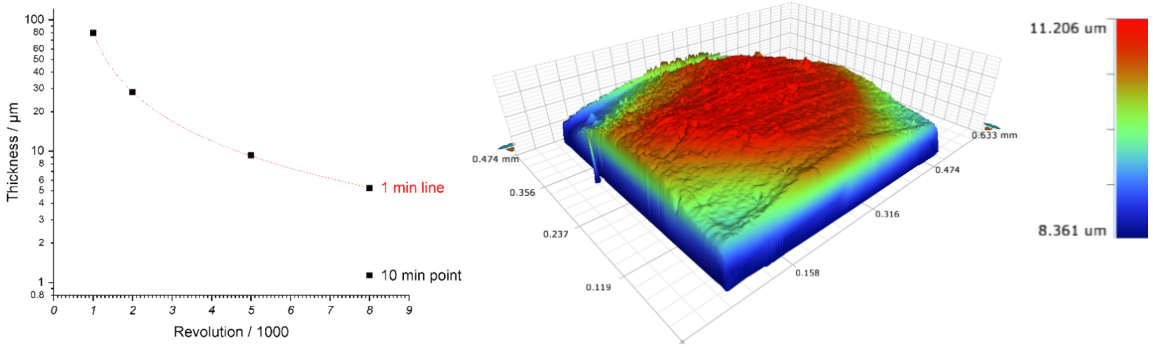

Figure S4 (left) Calibration curve for film thickness for spin coater speed and time.
(right) Heat map plot of the surface of a PDMS spin-coated NHA, spun at 5000 RPM for 2 min.

speeds and coating times using an optical profiler (Contour GT-X, Bruker). **Figure S4** shows the obtained calibration curve and 3D profile of the PDMS film of the nanohole array used for the experiment. Note that the vertical axis is on an expanded scale compared to the in-plane dimensions. The PDMS film in the experiments forms a smooth surface and has a thickness of 10.2 µm with a range of 2.8 µm. We observed a 10% variation in PDMS layer thickness for 5 different devices that were spin-coated in similar ways (5000 rpm for 2 mins). The largest variation in thickness within each sample was at the edge of the grid. This local variation in thickness does not influence the EOT resonance wavelength but may play a small role in the measured diffusion coefficients for a given analyte.

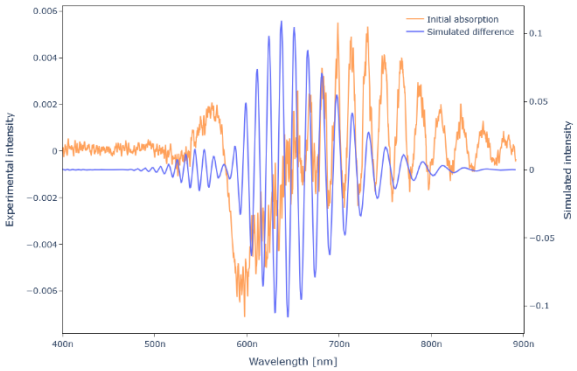

Figure S6 Differential spectrum after the first absorption stage (orange) and the modelled spectrum from Eq. * MERGEFORMAT (S 2) with a swelling of 3%. The shape of the experimental curve below 650 nm is due to the peak shift of the EOT resonance.

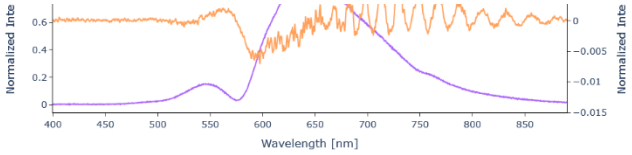

Figure S5 (top) Centroid shift for a full absorption and desorption run as in Figure 6 of the main text. (bottom) The normalized difference in intensity between the average intensity of the spectra in the ROI (10s window highlighted in green) and a reference region (highlighted in red). The differential spectrum was smoothed using a Savitz-Golay filter with a window size of 11 and polynomial order of 3.

5. Estimate of swelling using thin-film interferometry

The EOT spectra obtained prior to analyte uptake and after the initial rapid shift of the EOT centroid were subtracted to obtain a difference spectrum. The difference spectrum contains the expected derivative line shape near the EOT maximum but also amplifies the effect of thin film interference arising from Fresnel reflections at the PDMS interface. (**Figure S5**). These small oscillations suggest that a low finesse cavity is formed due to the thin film of PDMS. Specifically, the oscillations in the difference spectrum arise from the swelling of this layer, thus altering the thickness of the cavity.

These oscillations can be modelled using a transfer-matrix approach[1] where we consider a three-layer system consisting of a PDMS film suspended in air. In this situation, we have the top layer and bottom with a refractive index of n_1, with a second layer of thickness d with refractive index of n_2. For light with incident angle of θ, we can derive the phase accumulated through the second layer using Snell's law:

$$\varphi = \frac{2\pi n_2 d}{\lambda}\cos\theta \qquad \text{* MERGEFORMAT (S 1)}$$

The total transmission through the film is obtained by summing the infinite series of multiple reflected beams and given by:

$$t = \frac{4n_1 n_2 \exp(-j\varphi)}{(n_1+n_2)^2 - (n_1-n_2)^2 \exp(-j2\varphi)} \qquad \text{* MERGEFORMAT (S 2)}$$

To simulate the effects of swelling with the Fabry-Perot cavity in the difference spectrum, we adjust the thickness, *d*, and obtain the differential spectrum from the initial spectrum at the start of the sorption runs, i.e. before swelling had occurred.

Figure S6 shows the comparison of the experiment differential spectrum with that predicted by Eq. * MERGEFORMAT (S 1) and * MERGEFORMAT (S 2). The Figure qualitatively shows good agreement assuming swelling by 3 % upon uptake of o-xylene. The model does not show the experimental variation below 660 nm as * MERGEFORMAT (S 2) ignores the plasmonic interaction due to the nanohole array and the resulting EOT peak shift. The small difference between the location of the calculated and experimental minima may be explained by our assumption of an ideal and perfectly flat PDMS surface (**Figure S4**).

6. Diffusion kinetics for films mounted on impermeable or permeable substrates

The diffusion kinetics into either a film mounted on an impermeable support or of a free-standing film were derived by Crank in his book "The Mathematics of Diffusion" in 1956.[2] He solved Fick's second law of diffusion

$$\frac{\partial X}{\partial t} = D\frac{\partial^2 X}{\partial y^2}$$ * MERGEFORMAT (S 3)

for different cases, where D is the diffusion constant. Crank integrated this partial differential equation through the method of separation of variables

$$X(y,t) = C(y)T(t)$$ * MERGEFORMAT (S 4)

This method generates a general solution of the form:

$$X(y,t) = \sum_{m=1}^{\infty}(A_m \sin\lambda_m y + B_m \cos\lambda_m y)\exp(-\lambda_m^2 Dt)$$ * MERGEFORMAT (S 5)

We can determine the constants A_m, B_m, λ_m using the respective boundary and initial conditions for different cases. As described in the main text we need to solve * MERGEFORMAT (S 5) for boundary conditions representing a thin film mounted on either a permeable or an impermeable support, with the concentration being the analyte mole fraction, *X*.

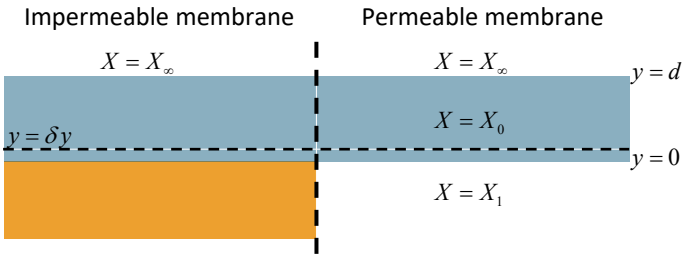

Figure S7 Boundary conditions for the impermeable and permeable membrane. In the case of the nanohole array, the impermeable membrane represents the PDMS supported by the gold layer, while the permeable membrane refers to the holes of the NHA.

6.1. Film on an impermeable support

The impermeable support model represents the common case of a flat and thin extraction matrix that is supported by a substrate. Many diffusion models in solid-phase micro-extraction but also many common matrices interrogated by interferometers are described by this model.[3, 4] Crank recast the system to have a symmetry plane, i.e. he considered a plane sheet of thickness $2d$, whose surface concentration is maintained at X_∞, and there is no diffusion across the central plane of the sheet.[2] With that assumption the boundary conditions become:

$$X = X_\infty, \qquad y = d, \qquad t \geq 0,$$ * MERGEFORMAT (S 6)

$$\partial X / \partial y = 0, \qquad y = 0, \qquad t \geq 0.$$ * MERGEFORMAT (S 7)

Saunders *et al.* showed that the solution for this problem is given by:[3]

$$X(y,t) = X_\infty\left(1 - \frac{4}{\pi}\sum_{n=0}^{\infty}\frac{(-1)^n}{2n+1}\exp\left\{-D(2n+1)^2\pi^2 t/4d^2\right\}\cos\frac{(2n+1)\pi y}{2d}\right)$$ * MERGEFORMAT (S 8)

In case of absorption into the supported film, we can determine the average concentration of the analyte within a thin slice (between y_1 and y_2) of the impermeable substrate by taking the integral of Eq. * MERGEFORMAT (S 8)*:*

$$\overline{X}(t) = \frac{1}{y_2 - y_1}\int_{y_1}^{y_2} X(y,t)\,dy$$ * MERGEFORMAT (S 9)

This integral evaluates to:

$$\overline{X}(t) = X_\infty\left(1 - \frac{8d}{(y_2 - y_1)\pi^2}\sum_{n=0}^{\infty}\frac{(-1)^n}{(2n+1)^2}\exp\left(-\frac{D\pi^2(2n+1)^2(t-t_0)}{4d^2}\right)\left[\sin\left(\frac{(2n+1)\pi y_2}{2d}\right) - \sin\left(\frac{(2n+1)\pi y_1}{2d}\right)\right]\right)$$ * MERGEFORMAT (S 10)

In our case we consider the plasmonic interaction near the metal dielectric interface ($y_1 = 0$; $y_2 = \delta y$) and the equation for the absorption kinetics becomes:

$$\overline{X}(t) = X_\infty\left(1 - \frac{8d}{\pi^2 \partial y}\sum_{n=0}^{\infty}\frac{(-1)^n}{(2n+1)^2}\exp\left(-\frac{D\pi^2(2n+1)^2(t-t_0)}{4d^2}\right)\sin\left(\frac{(2n+1)\pi\partial y}{2d}\right)\right) \quad \backslash^* \text{ MERGEFORMAT (S 11)}$$

We note that many other diffusion measurements determine the concentration through the evaluation of a material property (mass, density, refractive index) across the entire film ($y_1 = 0, y_2 = d$). The average analyte concentration across the entire film thickness then evaluates to:

$$\overline{X}(t) = X_\infty\left(1 - \frac{8}{\pi^2}\sum_{n=0}^{\infty}\frac{1}{(2n+1)^2}\exp\left(-\frac{D\pi^2(2n+1)^2(t-t_0)}{4d^2}\right)\right) \quad \backslash^* \text{ MERGEFORMAT (S 12)}$$

To describe the desorption process, $X_0 = X_\infty, X_1 = 0, X_2 = 0$ and * MERGEFORMAT (S 11) is written as:

$$\overline{X}(t) = X_\infty\left(\frac{8d}{\pi^2 \partial y}\sum_{n=0}^{\infty}\frac{(-1)^n}{(2n+1)^2}\exp\left(-\frac{D\pi^2(2n+1)^2(t-t_0)}{4d^2}\right)\sin\left(\frac{(2n+1)\pi\partial y}{2d}\right)\right) \quad \backslash^* \text{ MERGEFORMAT (S 13)}$$

6.2. Free-standing film (permeable support)

This case has not been discussed explicitly before in the literature but can be described in analogy to the case of the supported membrane. The boundary conditions are now given by:

$$X = X_1, \qquad y = 0, \qquad t \geq 0, \quad \backslash^* \text{ MERGEFORMAT (S 14)}$$

$$X = X_2, \qquad y = d, \qquad t \geq 0, \quad \backslash^* \text{ MERGEFORMAT (S 15)}$$

$$X = X_0, \qquad 0 < y < d, \qquad t \geq 0, \quad \backslash^* \text{ MERGEFORMAT (S 16)}$$

The solution to the differential equation * MERGEFORMAT (S 3) using * MERGEFORMAT (S 5) is then given by:

$$X(y,t) = X_1 + (X_2 - X_1)\frac{y}{d} + \frac{2}{\pi}\sum_{n=1}^{\infty}\frac{X_2\cos n\pi - X_1}{n}\sin\frac{n\pi y}{d}\exp\left(-\frac{Dn^2\pi^2 t}{d^2}\right) + \frac{4X_0}{\pi}\sum_{m=0}^{\infty}\frac{1}{2m+1}\sin\frac{(2m+1)\pi y}{d}\exp\left(-\frac{D(2m+1)^2\pi^2 t}{d^2}\right) \quad \backslash^* \text{ MERGEFORMAT (S 17)}$$

Similar to a film mounted in an impermeable support, we can find the average analyte concentration within a region defined by y_1 and y_2 by integrating * MERGEFORMAT (S 17):

$$\overline{X}(t) = X_1 + \frac{1}{y_2 - y_1}\left[\begin{array}{c}\frac{(X_2 - X_1)}{2d}\left(y_2^2 - y_1^2\right) - \frac{2d}{\pi^2}\sum_{n=1}^{\infty}\frac{X_2\cos n\pi - X_1}{n^2}\left(\cos\frac{n\pi y_2}{d} - \cos\frac{n\pi y_1}{d}\right)\exp\left(-\frac{Dn^2\pi^2 t}{d^2}\right) \\ -\frac{4dX_0}{\pi^2}\sum_{m=0}^{\infty}\frac{1}{(2m+1)^2}\left(\cos\frac{(2m+1)\pi y_2}{d} - \cos\frac{(2m+1)\pi y_1}{d}\right)\exp\left(-\frac{D(2m+1)^2\pi^2 t}{d^2}\right)\end{array}\right] \backslash^*$$

MERGEFORMAT (S 18)

Considering the boundary conditions $X_0 = 0, X_1 = 0, X_2 = X_\infty$, the equation for the absorption process becomes:

$$\overline{X}(t) = X_\infty\left[\frac{\left(y_2^2 - y_1^2\right)}{2d\left(y_2 - y_1\right)} - \frac{2d}{\left(y_2 - y_1\right)\pi^2}\sum_{n=1}^{\infty}\frac{(-1)^n}{n^2}\left(\cos\frac{n\pi y_2}{d} - \cos\frac{n\pi y_1}{d}\right)\exp\left(-\frac{Dn^2\pi^2 t}{d^2}\right)\right] \quad \backslash^* \text{ MERGEFORMAT (S 19)}$$

Within the range of the plasmonic interaction ($y_1 = 0$; $y_2 = \delta y$), we obtain the simple expression:

$$\overline{X}(t) = X_\infty\left[\frac{\partial y}{2d} - \frac{2d}{\partial y\pi^2}\sum_{n=1}^{\infty}\frac{(-1)^n}{n^2}\left(\cos\frac{n\pi\partial y}{d} - 1\right)\exp\left(-\frac{Dn^2\pi^2 t}{d^2}\right)\right] \quad \backslash^* \text{ MERGEFORMAT (S 20)}$$

For the desorption case, we can, again, consider the case when the initial conditions are given by $X_0 = X_\infty, X_1 = 0, X_2 = 0$. Within the range of the plasmonic interaction, we obtain:

$$\overline{X}(t) = X_\infty \left[\frac{4d}{\partial y \pi^2} \sum_{n=0}^{\infty} \frac{1}{(2n+1)^2} \left(1 - \cos \frac{(2n+1)\pi \partial y}{d} \right) \exp\left(-\frac{D(2n+1)^2 \pi^2 t}{d^2} \right) \right] \quad \backslash\text{* MERGEFORMAT (S 21)}$$

Integrating instead over the entire film, $y_1 = 0, y_2 = d$ the average analyte concentration is given by

$$\begin{aligned} \overline{X}(t) &= X_\infty \left[\frac{1}{2} - \frac{2}{\pi^2} \sum_{n=1}^{\infty} \frac{1}{n^2} \left(1 - (-1)^n \right) \exp\left(-\frac{Dn^2 \pi^2 t}{d^2} \right) \right] \\ &= X_\infty \left[\frac{1}{2} - \frac{2}{\pi^2} \sum_{m=0}^{\infty} \frac{2}{(2m+1)^2} \exp\left(-\frac{D(2m+1)^2 \pi^2 t}{d^2} \right) \right] \end{aligned} \quad \backslash\text{* MERGEFORMAT (S 22)}$$

in analogy to * MERGEFORMAT (S 12). A detailed discussion of these cases will be given in a forthcoming publication.

7. Diffusion constants

The data tables below shows the absorption (Table 1) and desorption (Table 2) diffusion constants and coefficients obtained by fitting the experimental data to equation (8) of the main text. The data are displayed in Figure 7 of the main text.

Table 1 Absorption diffusion constants and limiting asymptotic concentrations for each diffusion process

Flow rate [µL/min]	Partial pressure [Pa]	Concentration [ppm]	Diffusion constant, D_1 [cm^2s^{-1}]	Asymptotic concen., X_1 [mol. frac]	Diffusion constant, D_2 [cm^2s^{-1}]	Asymptotic concen., X_2 [mol. frac]
2	59	590	(17 ± 3) x 10^{-9}	1.5 x 10^{-3}	(5 ± 2) x 10^{-9}	1.4 x 10^{-3}
3	89	885	(20 ± 1) x 10^{-9}	3.1 x 10^{-3}	(3 ± 2) x 10^{-9}	0.5 x 10^{-3}
4	120	1180	(18 ± 2) x 10^{-9}	2.6 x 10^{-3}	(6 ± 3) x 10^{-9}	0.6 x 10^{-3}
5	149	1470	(20 ± 2) x 10^{-9}	3.1 x 10^{-3}	(3 ± 1) x 10^{-9}	0.9 x 10^{-3}
6	179	1770	(20 ± 2) x 10^{-9}	3.1 x 10^{-3}	(0.4 ± 0.2) x 10^{-9}	3.4 x 10^{-3}
7	209	2060	(21 ± 2) x 10^{-9}	3.2 x 10^{-3}	(0.6 ± 0.3) x 10^{-9}	3.4 x 10^{-3}
8	239	2360	(24 ± 0.4) x 10^{-9}	3.2 x 10^{-3}	(0.5 ± 0.1) x 10^{-9}	4.4 x 10^{-3}
9	269	2650	(27 ± 3) x 10^{-9}	3.7 x 10^{-3}	(0.8 ± 2) x 10^{-9}	4.6 x 10^{-3}
10	298	2940	(24 ± 4) x 10^{-9}	3.3 x 10^{-3}	(0.9 ± 0.2) x 10^{-9}	4.5 x 10^{-3}

Table 2 Desorption diffusion constants and limiting asymptotic concentrations for each diffusion process

Flow rate [µL/min]	Partial pressure [Pa]	Concentration [ppm]	Diffusion constant, D_1 [cm^2s^{-1}]	Asymptotic concen., X_1 [mol. frac]	Diffusion constant, D_2 [cm^2s^{-1}]	Asymptotic concen., X_2 [mol. frac]
2	59	590	(17 ± 4) x 10^{-9}	1.8 x 10^{-3}	(2.9 ± 0.3) x 10^{-9}	0.8 x 10^{-3}
3	89	885	(12 ± 2) x 10^{-9}	2.2 x 10^{-3}	(2.1 ± 0.4) x 10^{-9}	0.9 x 10^{-3}
4	120	1180	(9 ± 1) x 10^{-9}	2.1 x 10^{-3}	(1.7 ± 0.2) x 10^{-9}	0.9 x 10^{-3}
5	149	1470	(6 ± 2) x 10^{-9}	1.6 x 10^{-3}	(2.9 ± 0.6) x 10^{-9}	1.2 x 10^{-3}

6	179	1770	(7 ± 2) x 10^{-9}	1.7 x 10^{-3}	(2.3 ± 0.5) x 10^{-9}	1.6 x 10^{-3}
7	209	2060	(20 ± 10) x 10^{-9}	2.2 x 10^{-3}	(2.1 ± 0.6) x 10^{-9}	1.6 x 10^{-3}
8	239	2360	(58 ± 3) x 10^{-9}	3.4 x 10^{-3}	(2.9 ± 0.7) x 10^{-9}	3.2 x 10^{-3}
9	269	2650	(47 ± 4) x 10^{-9}	3.7 x 10^{-3}	(2.4 ± 0.1) x 10^{-9}	3.3 x 10^{-3}
10	298	2940	(41 ± 4) x 10^{-9}	3.5 x 10^{-3}	(2.3 ± 0.1) x 10^{-9}	3.3 x 10^{-3}

The diffusion constants for the absorption processes are averaged to D_1 = (22 ± 6) x 10^{-9} $cm^2s^{-1}$and D_2 = (0.9 ± 1.5) x 10^{-9} cm^2s^{-1}, whereas averaging the diffusion constants for the desorption processes yields D_1 = (29 ± 21) x 10^{-9} cm^2s^{-1} and D_2 = (2.5 ± 0.7) x 10^{-9} cm^2s^{-1}.

Here, the average was determined from the average of the diffusion constants weighted by their relative contribution to the process.

$$\bar{D}_i = \frac{\sum_n X_{i,n} D_i}{\sum_n X_{i,n}} \qquad \text{* MERGEFORMAT (S 23)}$$

The associated uncertainty

$$\sigma\left(\bar{D}_i\right) = \sqrt{S\left(\bar{D}_i\right)^2 + \Delta\bar{D}_i^2} \qquad \text{* MERGEFORMAT (S 24)}$$

was determined from the respective weighted uncertainties of each of the measurement $\Delta D_{1,2}$, and from the standard deviation of the measured diffusion constants $S(D_{1,2})$

$$\Delta\bar{D}_i = \frac{\sum_n X_{i,n}\Delta D_{i,n}}{\sum_n X_{i,n}}; S\left(\bar{D}_i\right) = \sqrt{\frac{\sum_n X_{i,n}\left(D_{i,n} - \bar{D}_i\right)^2}{\sum_n X_{i,n}}} \qquad \text{* MERGEFORMAT (S 25)}$$

8. FDTD simulation: electric field distribution across the NHA film

The spatial distribution of the electric field generated by the surface plasmon polaritons was determined by FDTD and was used to estimate the fraction of intensities inside and outside of the holes. This was achieved by applying a mask of the hexagonal pattern of the array on the spatial field distribution at different depths into the PDMS layer. From **Figure S8**, we can see that within

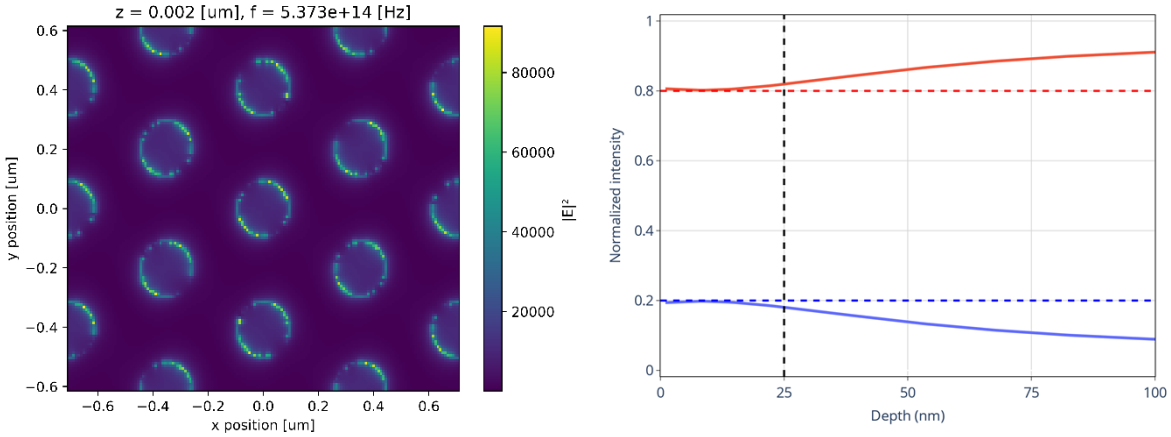

Figure S8 (left) Spatial electric field distribution over the nanohole at the Au-PDMS interface. (right) Plot of fraction of averaged intensities inside (solid blue) and outside (solid red) the holes of the NHA surface for different depths. The dashed red and blue lines represent the values used for modelling the diffusion kinetics as a linear combination of the two contributions. The dashed black line represents the penetration depth of the evanescent wave into the PDMS layer.

the range of the plasmonic interaction (δy = 25 nm), the ratio of intensity outside versus inside the holes is close to 4:1, consistent with the ratio of areas used for the modelling of diffusion coefficients in equation (7) of the main text.

References

1. B. E. A. Saleh and M. C. Teich, *Fundamentals of photonics*, Wiley-Interscience, Hoboken, N.J, 2nd edn., 2007.
2. J. Crank, *The Mathematics of Diffusion*, Oxford University Press, New York, 2nd Edition edn., 1990.
3. J. E. Saunders, H. Chen, C. Brauer, M. Clayton and H. P. Loock, *Soft Matter*, 2018, **14**, 2206-2218.
4. J. E. Saunders, H. Chen, C. Brauer, M. Clayton, W. Chen, J. A. Barnes and H.-P. Loock, *Soft Matter*, 2015, **11**, 8746-8757.